



HAL
open science

Strong magnetocaloric effect induced by spin reorientation transitions in epitaxial Ho thin films

O. Koplak, R. Morgunov, R. Medapalli, E. Fullerton, S Mangin

► **To cite this version:**

O. Koplak, R. Morgunov, R. Medapalli, E. Fullerton, S Mangin. Strong magnetocaloric effect induced by spin reorientation transitions in epitaxial Ho thin films. *Physical Review B*, 2020, 102, pp.134426. 10.1103/physrevb.102.134426 . hal-03042896

HAL Id: hal-03042896

<https://hal.univ-lorraine.fr/hal-03042896v1>

Submitted on 7 Dec 2020

HAL is a multi-disciplinary open access archive for the deposit and dissemination of scientific research documents, whether they are published or not. The documents may come from teaching and research institutions in France or abroad, or from public or private research centers.

L'archive ouverte pluridisciplinaire **HAL**, est destinée au dépôt et à la diffusion de documents scientifiques de niveau recherche, publiés ou non, émanant des établissements d'enseignement et de recherche français ou étrangers, des laboratoires publics ou privés.

Strong magnetocaloric effect induced by spin reorientation transitions in epitaxial Ho thin films

O. Koplak¹, R. Morgunov^{1,2}, R. Medapalli^{3,4}, E. Fullerton³, S. Mangin⁵

¹*Institute of Problems of Chemical Physics, 142432, Chernogolovka, Russia*

²*I.M. Sechenov First Moscow State Medical University, Ministry of Health of Russia, 119991 Moscow, Russia*

³*Center for Memory and Recording Research, University of California, San Diego, California 92093-0401, USA*

⁴*Department of Physics, School of Sciences, National Institute of Technology, Andhra Pradesh-534102, India*

⁵*Université de Lorraine, CNRS, IJL, F-54000 Nancy, France*

*E-mail: o.koplak@gmail.com

Magnetocaloric effect (MCE) in antiferromagnetic holmium (Ho) film is studied near the spin reorientation temperatures. A series of magnetization isotherms from 60 K to 150 K around the Neel temperature, $T_N \approx 130$ K were recorded for both in-plane and out-of-plane magnetic field orientations. A change in entropy, ΔS_M of -5 J/kg K was found near T_N for an in-plane field orientation. A large change in ΔS_M of -11.8 J/kg K due to a fan-helix spin transition at $T = 90$ K is observed for an in-plane field orientation. Spin transition at both T_N and at the fan-helix transition exhibit larger MCE in the in-plane field orientations in comparison with the perpendicular orientation. The value of the refrigerant capacity extracted from the temperature dependence of $\Delta S_M(T)$ is found to be larger for the "in-plane" orientation by a factor of two.

I. INTRODUCTION

Holmium (Ho) is a rare earth spiral antiferromagnet, where the magnetic moments in each of its atomic layers align in-plane to form a ferromagnetic state, but each layer is slightly misaligned to each adjacent layer resulting in an out-of-plane helix magnetic structure. Ho has a commensurate conical structure below $T_C \sim 19$ K and a basal-plane spiral structure between 19 K and 133 K in their helicities. Above the Néel temperature (T_N) ~ 133 K, Ho is paramagnetic [1–4]. Several magnetic phases (cone, fan, and helix) exist at different temperatures in zero magnetic field. Such magnetic phases have been extensively studied and well understood. However, application of an external magnetic field has a huge influence on formation various intermediate magnetic phases, e.g., spin-slip, ferrofan, and helifan. The existence of each phase is determined by two major competing energies: exchange and magneto-crystalline anisotropy. For instance, in high-purity holmium crystals the spin-slip and fan-helicoidal phases can be observed [1–4]. In [5], the region of existence of a spin-slip phase in the 95 – 110 K range and an intermediate phase of the ferro-fan type in the 40 – 120 K range were found under 20 – 80 kOe applied magnetic field. In zero field at $T = 78$ K, the spin-slip phase turns into a spiral phase. Moreover, in Ho thin films the (H, T) phase diagram is highly affected by strain of the films on the substrate, mechanical stress and thickness limitation [6], which can strongly influence the crystallographic structure [7], and the direction of the easy axis of magnetization [8]. Decreasing the Ho film thickness suppresses spin structure, which are becoming energetically unfavorable in thin films [6]. All mentioned above spin transitions can be used to develop magnetocaloric effect (MCE). Special attention will be focused to magnetic anisotropy of spin structures and tuning of the favorable field orientation to maximize the MCE. Therefore, our

work is aimed to study the anisotropy of MCE in MgO/W/Ho/W multilayer structure, with Ho grown along the c -axis (0002) with a thickness of 400 nm intermediate to bulk and thin film limit. The thickness was chosen to conserve presence of all known spin phases. From the evolution of M as a function of H for temperatures between 60 – 100 K we could calculate two significant variations of the magnetic part of entropy: one for $T_N = 133$ K and for the other $T = 90$ K. We will show that at these particular temperatures the entropy changes strongly dependent on the field orientation. At a magnetic phase transition (for example at T_C), the magnetization strongly varies in a narrow temperature range *i.e.* the value of $\partial M/\partial T$ is large. In theory first-order phase transition occurs at a fixed transition temperature, T_c and, thus, $(\partial M/\partial T)H$ value should be infinitely large. For example, giant magnetocaloric effect (GMCE) is associated with a first-order transition provided by a strong spin-lattice interaction [9, 10]. In the case of second-order magnetic phase transitions, the presence of short-range order and spin fluctuations above the ordering temperature leads to a decrease in the maximum possible value of $(\partial M/\partial T)H$ and MCE [11, 12]. Under the assumption that the metal goes from a completely disordered paramagnetic state to a fully ordered magnetic state in the temperature range considered, the magnetic entropy variation, during that particular transition, ΔS_M depends on multiplicity $2J+1$ where J is the total angular momentum and is given by:

$$\Delta S_M = R \ln(2J + 1) \quad (1),$$

Where R is the universal gas constant. As Ho, exhibits the largest J value of all the rare-earth elements, it is a natural candidate to study MCE. The theoretical value of the saturation moment in Bohr magnetons/atom is given by gJ (where $g = 5/4$, $J = 8$, and $gJ = 10 \mu_B/\text{atom}$). For rare earth elements, such as Ho, crystal electrical fields always lift the multiplicity $2J+1$ under huge single

ion anisotropy. This greatly reduces the entropy from the value estimated by expression (1). The experimental value of magnetic moment strongly depends on structure of Ho and crystallographic orientations. Due to the fact that Ho exhibits various magnetic phase transitions in the (H, T) space, one can expect that the MCE can be maximum at those particular transition temperatures [1-8]. Several studies have reported various spin structures in crystalline bulk Ho (see Fig. S1 in Supplementary material [13]) [14, 15]. However, the MCE in Ho films is practically not analyzed in the literature.

II. EXPERIMENTAL TECHNIQUE AND SAMPLES

Using magnetron sputtering technique, we deposited 400 nm thick Ho thin film on single crystalline MgO substrates with an intermediate buffer layer of tungsten W. Deposition of W onto MgO (100) first yields W(100) growth which sets an epitaxial growth in Ho with its c -axis (0002) normal to the sample plane. In [17] high crystallinity of the epitaxial films was confirmed by very narrow rocking curves peaks with the full width at half maximum $\Delta\theta < 2^\circ$ indicative of a high degree of crystalline orientation. We used the samples grown in the same machine with the same growth protocol. A 5 nm thick W film was used to protect the Ho film from oxidation. Prior to deposition of the films, the substrate was baked at 800 °C for 45 min, and then at 700 °C for 30 min after which a 10 nm thick W film was deposited at the same temperature. Subsequently, the specimen was cooled to room temperature where a 400 nm thick Ho film was deposited, and further annealed at 500 °C from 45 mins to ensure a crystalline growth in Ho. The sample was then capped with a 5 nm thick W layer while cooling to room temperature. Similar epitaxial growth of Ho film on W substrate was achieved by Wescke *et al.* [16]. The Ho film with a thickness of 400 nm corresponds to ~ 60 periods of spin-helix rotation (each period is 12 lattice parameters 5.6 Å along c axis) in the bulk Ho. Thus, the thickness exceeds the spin-structure period and allows one to find effect of the mechanical stresses on known transitions. A study based on neutron diffraction technique has shown that even 100 nm films do not correspond to bulk properties and still convenient to study periodicity of spin helix and other incommensurate spin structures [18].

Several techniques were used to characterize the heterostructure: X-Ray Diffraction (XRD) for structural analysis, X-ray photoelectron spectroscopy (XPS) for surface investigations and energy dispersive X-ray (EDX) spectroscopy for layer-by-layer analysis. Structural analysis was performed by a Bruker X-ray diffractometer providing 2θ -scanning under $\text{CuK}\alpha_1$ -irradiation. Scanning step was 0.02° . The chemical composition of subsurface layers of the films was determined by X-ray photoelectron Specs Phoibos HSA 3500 spectrometer in 10^{-9} mbar vacuum. Local chemical composition determined by energy dispersive analysis as well as images of surface were recorded by a SUPRA 25 Zeiss electron microscope with different accelerating voltages. Magnetization as an H and T were recorded using MPMS XL Quantum Design SQUID magnetometer in the range of $T = 2\text{-}300$ K for external magnetic applied along “in-plane” and

“out-of-plane” orientations. In the vicinity of phase transitions, isothermal $M(H)$ curves were measured at a fixed cryostat temperature for ranging between 60 - 150 K with a 5 K step.

III. RESULTS AND DISCUSSION

A. Structural and chemical analysis of the sample

The XRD spectrum of the analyzed film and simulated spectrum of single crystal Ho are shown in Fig. 1(a) and 1(b), respectively. The MgO and W peaks, the Ho(002) and (004) reflections are observed indicating c -axis growth. Holmium lattice corresponds to P63/mmc space group, hexagonal close-packed structure with cell parameters: $a = 3.5773$ Å, $b = 3.5773$ Å, $c = 5.6158$ Å. X-ray diffraction results for Ho grown onto MgO(111) substrates with W(110) buffer layers (Fig.1 (a)). Dominating intensity of narrow Ho(002) peak, positions of the (002) and (004) peaks coinciding with ones recorded in [17] verify single crystallinity of the film used in our experiments. The spectrum in Fig.(1a) is rather different from ones recorded for nanocrystalline and coarse-grain Ho films [19] and theoretically calculated Ho powder spectrum (Fig.(1b)) [20]. Theoretical calculation of spectrum in Fig. 1b was fulfilled by Crystallography Open Database [20]. Powder patterns were obtained for hexagonal lattice space group P63/mmc with atomic coordinates in elementary cell $x = 0.333$, $y = 0.667$, $z = 0.250$. Full description including references and CIF file is presented in [20]. Plot of the spectrum in Figure 1b was performed by Match software downloading data from Crystallography Open Database [20].

Clearly it seen the presence of a mechanical stress in the Ho films as shift of the positions of Ho(002) and (004) peaks in comparison with its positions in the simulated XRD spectrum (Fig.(1b)) and insertion in Fig.(1a). The full width at half maximum $\Delta\theta < 1^\circ$ was even smaller, that in [17] indicating a high degree of crystalline orientation.

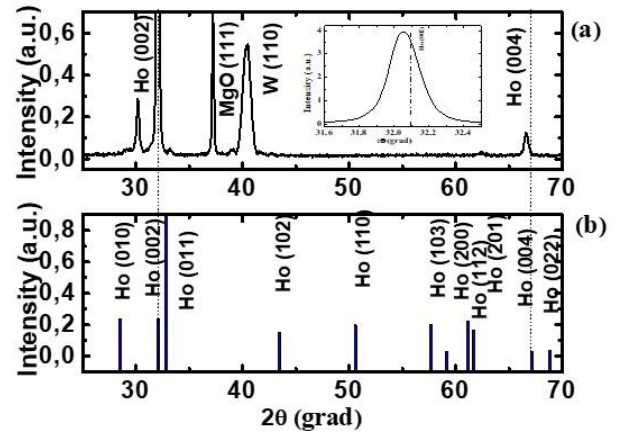


FIG.1. (a) X-ray diffraction spectrum measured in MgO/W(10 nm)/Ho(400 nm)/W(5 nm) sample, (b) simulation of Ho powder X-ray spectra obtained using Crystallography Open Database [20]. Vertical dashed lines indicate positions of the Ho(002) and (004) reflections in simulated spectrum. Shift of the Ho(002) line from calculated position is shown in insertion.

Probably this indicates a mechanical stress, which can affect critical temperatures at which the spin transitions are observed as

well as the MCE in epitaxial films in comparison with the bulk systems [21].

With the aid of surface sensitive XPS analysis we verified the electronic states of Ho and its possible oxidation and presence of the declared chemical elements (see Fig. S2 in the Supplementary material [13]). The XPS spectrum shown in Fig. S2(a) in the Supplementary material [13] demonstrates a presence of W and Ho main elements in sample. The O and C peaks has no relation to the sample and correspond to unavoidable impurities in spectrometer. In the insertion in the Fig. S2(a) in the Supplementary material [13], the peak at $E_e = 159.6$ eV corresponds to $4d$ electronic level of Ho^{3+} ion in $1^{10}(^5I_8)$ ground state. One can conclude the absence of the oxygen and carbon in Ho layer. Zoomed spectrum of W $4d$ -core level is presented in Fig. S2(b) in the Supplementary material [13]). Presence of the pure W as well as its oxidation was confirmed by few O 1s peaks see insertion in Fig. S2(b) Supplementary material [13]. Magnesium oxide was not detected due to lower penetration depth ($\sim 5-7$ nm) of X-ray.

Layer by layer chemical analysis of the sample was performed by EDX spectroscopy, and the measured spectrum is shown in Fig. S3(a) Supplementary material [13]. The EDX spectrum was collected in the area marked by pink rectangle in the inset of Fig. S3(a). Clearly, the spectrum indicates the presence of W, Ho, Mg, O, C elements similarly with XPS technique (Fig. S3(a)). The EDX technique with different accelerating voltage made it possible to estimate the percentage ratio of chemical elements dependently on the beam penetration depth peaks Sketch of experiments is shown on the Supplementary material [13], insertion in Fig. S3(b)). Since analyzing sample has multilayered structure, the estimation was complicated by back scattering in interfaces and depends film thickness at low accelerating voltages. We used enhanced voltage 7 - 25 keV to reach all layers of the sample (Fig. S3(b)). We plotted depth distribution of the chemical elements based on calculated R values (Fig. S3(b)). We applied Bethe formula and Kanaya-Okayama expression [22] to calculate penetration depth of electrons R as function of their energy E . Presence of the chemical elements in corresponded layers was verified. We can see approximate EDX determined values of the Ho thicknesses ~ 400 nm which is in good agreement with estimations of thickness by deposition time (see Fig. S3(c) in the Supplementary material [13]).

B. Orientation and temperature dependence of hysteresis loops

Figure 2 shows two magnetic hysteresis loops for the in-plane and out-of-plane orientations of the applied magnetic field at 2 K are presented. When the field is applied in the plane of the sample, the hysteresis loop has a rectangular shape with $M_r/M_s = 0.78$, where M_r is the remnant magnetic moment, M_s is saturation magnetic moment. In the out-of-plane orientation, $M(H)$ shows almost no hysteresis and $M_r/M_s = 0.1$. Detailed magnetic hysteresis loop of the $\text{MgO}/\text{W}/\text{Ho}(400\text{ nm})/\text{W}$ structure for in-plane orientations is shown in Fig. 3. The shape of the $M(H)$ curve changes as temperature of the sample is varied. In a temperature

range of 70-100 K, magnetization jumps appeared in $M(H)$ curves due to spin transitions (Fig. 3).

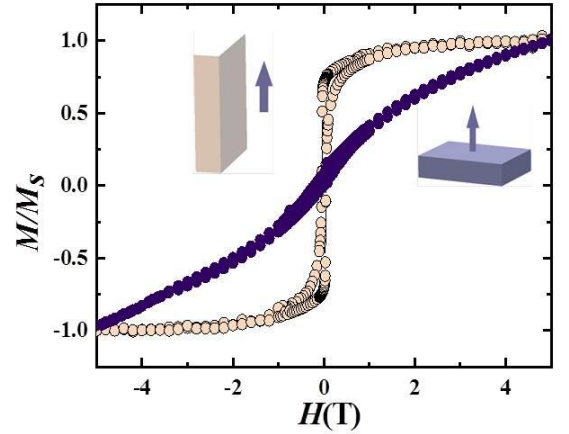


FIG.2. Normalized magnetization (M/M_s) as a function of H curves for in-plane (beige) and out-of-plane (violet) applied field orientations measured at 2 K are shown. Directions of the applied magnetic field are shown in the insets.

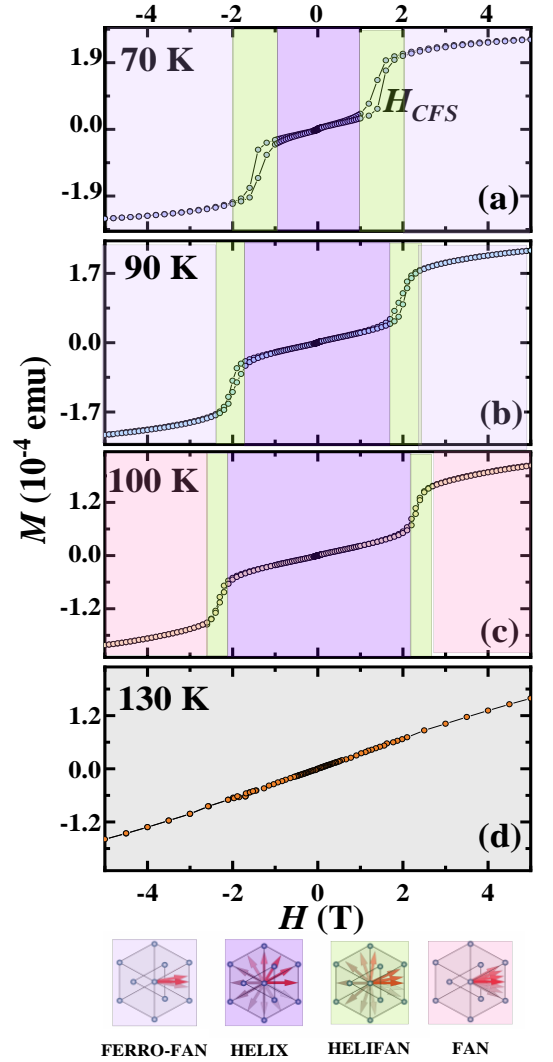


FIG.3. Magnetization as a function of the applied magnetic field measured in $\text{MgO}/\text{W}/\text{Ho}(400\text{ nm})/\text{W}$ sample at different temperature: 70 K (a), 90 K (b), 100 K (c) and 130 K (d). Note that the loops are measured in the in-plane orientation. Schematic

spin directions in the atomic layers corresponding to the spin phases are shown at the bottom.

Well known magnetic phases (ferrofan, helix, helifan, fan) are marked by colors in Fig. 3 and their corresponding schematics are presented in the bottom panel of Fig. 3. Above T_N , the sample takes a transition into the paramagnetic phase and this behavior is clearly evident from Fig. 3(d). In Figs. 3(a)-3(c), the in the magnetization correspond to a transition into a helifan phase.

An increase in the temperature causes widening of the helical phase region in H . Upper border of the helix phase with critical field switching H_{CFS} , shifts from $H_{CFS} = 1.57$ T at 70 K up to $H_{CFS} = 2.04$ T at 100 K (see Figs. 3 (a)-(c)). Simultaneously field ranges corresponding to the ferro-fan (violet), helifan (green) and fan (pink) rapidly decrease with an increase in the temperature. Finally, all magnetically ordered phases disappear and field dependencies transforms to the straight line near T_N (Fig. 3(d)). In the paramagnetic phase, the slope of the $M(H)$ straight line (Fig. 3 (d)) characterizes magnetic moment of the single Ho atom calculated by formula $\mu H (\delta\chi T)^{1/2} = 10 \mu_B$ normally relating to an individual Ho ion.

C. Anisotropy of the evolution of the magnetic moment as a function of temperature

Temperature dependencies of the magnetic moment under the influence of external magnetic field applied in-plane and out-of-plane are shown in Fig. 4(a) and Fig. 4(b), respectively.

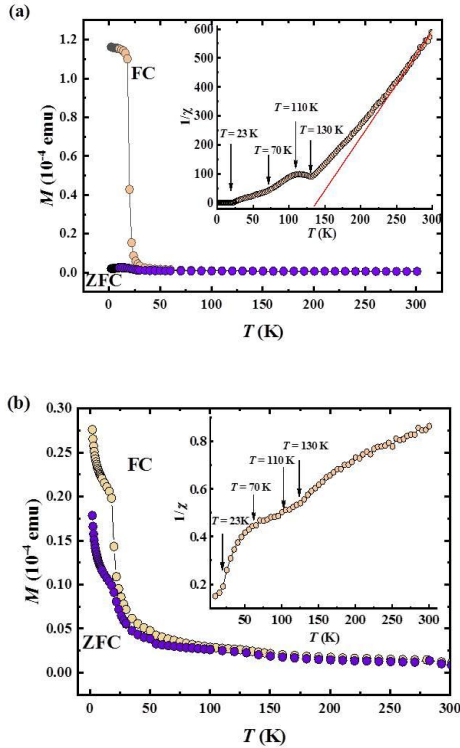


FIG.4. Magnetic moment as a function of temperature recorded under 100 Oe applied magnetic field in *FC*, *ZFC* modes for both in-plane applied field (a) and out-of-plane applied field (b) orientations. The temperature dependencies of the reciprocal magnetic susceptibility $1/\chi(T)$ are shown in the insets for both in-plane (a) and out-of-plane (b) orientations. Red line is approximation by Curie-Weiss law. Known spin reorientation transitions (ferrofan, helix, helifan, fan and spin-slip) at correspondent temperatures are indicated by arrows.

Two types of the temperature dependencies $M(T)$ are recorded for each orientation: 1) *FC* (Field Cooling) corresponds to the measurement of magnetic moment during sample heating in low magnetic field 100 Oe after a sample cooling in a strong 5 T field 2) *ZFC* (Zero Field Cooling) corresponds measurement of magnetic moment during sample heating in magnetic field 100 Oe after the cooling of sample in zero field.

The divergence of the *ZFC* curves at low temperature below 20-25 K corresponds to a first order phase transition (Fig. S 5 b) in agreement with previous investigations in literature [8]. Temperature of the magnetic ordering (transition between paramagnetic and helix phases) $T_N \approx 130$ K was determined as a maximum on $M(T)$ dependencies for the field in-plane and out-of-plane orientations (see Fig. 4(b)). These features are clearly seen in derivative plots $dM/dT(T)$ (see Fig. S4(b) in the Supplementary material [13]).

Reciprocal magnetic susceptibilities $1/\chi = 1/(dM/dH)$ for in-plane and out-of-plane applied field orientations are shown in the insets of Fig.4 in order to show the transitions at 130 K (paramagnet - helix), 110 K (helix - fan), 70 K (fan - ferrofan or fan-helifan) and low temperature transition at 23 K (ferrofan-cone) are shown by vertical arrows. We plotted high temperature tangent straight line intersecting on to the horizontal axis at $T = 130$ K to determine the Weiss temperature, $\Theta = 130$ K coinciding well with the critical temperature of the paramagnet-helix transition.

The value of the MCE strongly depends on the measurement procedure of the isothermal $M(H)$ curves [23]. Driving the sample through the phase transition in a mixed-phase state or stable state leads to a different value of MCE [23]. For instance, in this case, when the sample is abruptly cooled down to a lower temperature by 5 K or when heated to room temperature before next measurement the values of $M(H)$, and MCE differ by about 8 times [23]. In our experiment, the stepwise cooling was used before recording of the isothermal magnetization curves. A magnetic field of 5 T was applied from a temperature of 60 K to a temperature of 150 K by 5 K step increments in the in-plane and out-of-plane orientations (Fig. 5 a, b). The sample orientation was strictly fixed during recording of each set of $M(H)$ curves. Sample was not removed from magnetometer within the series of measurements (Fig. 5 a, b). Rotation of the sample in ab plane from orientation $H \parallel a$ to orientation $H \parallel b$ does not change field dependence $M(H)$ (see Figure S5 in the Supplementary material [13]), i.e. magnetization in ab plane is isotropic. Thus, anisotropy in ab plane is rather similar with XY-like model, than Ising model.

In order to subtract the demagnetization field $4\pi M_s = 1.7$ kOe at $H = 50$ kOe, all isothermal out-of-plane $M(H)$ curves were

corrected for the demagnetizing factor $N = 1$ [24] (see Fig.S6 in the Supplementary material [13]), while no corrections were needed for in-plane $M(H)$ curves. The isothermal magnetization $M(H)$ curves are shown in in-plane and out-of-plane orientations in Fig. 5(a) and Fig. 5(b), respectively for various temperatures of the sample in the range of 60 – 150 K.

In the in-plane orientation, the linear $M(H)$ dependence above 130 K gradually transforms into a stepwise curve at 130 K (see Fig. 5(a)). In the out-of-plane orientation, change of the curve shape occurs at 70 K (see Fig. 5(b)). Difference between the observed in-plane and out-of-plane critical temperatures can obviously be explained by correspondent phase transitions at 130 K and 70 K.

The comparison between the critical transitions temperatures in W/Ho(0002)/W film and Ho single crystal b -axis [8] is shown in Fig. S7 in the Supplementary material [13] on temperature dependencies of reciprocal magnetic susceptibilities $1/\chi$.

In order to characterize the type of transitions we observed in our experiment, we plotted Arrott curves $M^2(H/M)$, in the 60 - 150 K temperature range.

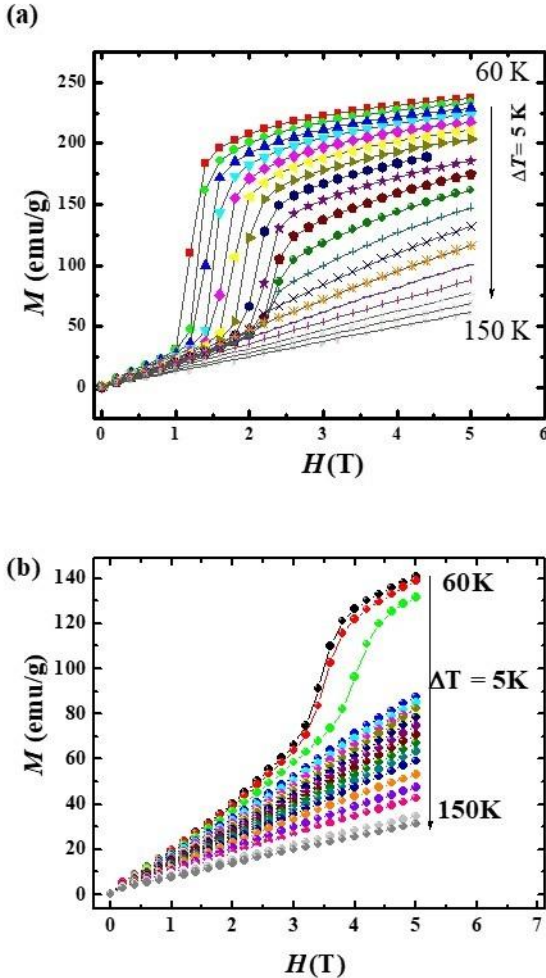


FIG.5. Magnetization as a function of the magnetic field for various temperatures. The field is applied (a) in-plane and (b) out-of-plane orientations. The curves are presented after performing the correction due to demagnetizing field.

Arrott technique is based on Weiss molecular field theory assuming a proportionality between the intrinsic magnetic field of the ferromagnet and its magnetization [25, 26]. According to Ginzburg-Landau mean field theory [25], the free energy of a ferromagnetic in the vicinity of phase (spin) transition can be expressed as:

$$F(M) = -HM + \alpha \frac{(T-T_c)}{T_c} M^2 + \beta M^4 \dots \quad (2)$$

Where HM is the Zeeman energy, the second and the third terms correspond to magnetization dependent intrinsic energies. In general, Arrott plot is based on Arrott–Noakes equation [26]:

$$(H/M)^{1/\gamma} = \frac{(T-T_c)}{T_c} + \left(\frac{M}{Mr}\right)^{1/\beta} \quad (3)$$

Where γ and β are the critical parameters associated with magnetic susceptibility and saturation magnetization, respectively. To apply Arrott analysis, the material should be magnetically homogeneous, i.e. the spin correlation length should be large enough in comparison with the range of structural inhomogeneity. In the frame of the mean field model, exponents $\beta = 0.5$, $\gamma = 1.0$ give straightening of the $M(H)$ curves around T_c corresponding to the long-range magnetic ordering, i.e. mean field model gives straight lines in M^2 on H/M coordinates. The curve slope $\varepsilon = (T-T_c)/T_c$ determines critical temperatures. The straight line crossing M^2 axis at $\varepsilon < 0$ corresponds to the temperature higher than the critical temperature, while the straight line crossing the H/M axis (at $\varepsilon > 0$) lies in temperature range below T_c . The line directed to zero point at $H = 0$ corresponds to critical temperature. Positive $M^2(H/M)$ slope indicates a second order transition, while negative slope corresponds to first order transition [26, 27]. The Arrott plots in M^2 vs H/M “mean-field” axis are presented in Fig. 6(a).

Clearly, the curves are non-linear. Since the narrow lines in the X-ray spectrum (see Fig. 1) confirm single crystalline structure of the film, curvature of the lines in Arrott plot cannot be explained by film structural inhomogeneity, which correlation length is shorter than magnetic correlation length. The values $\beta = 0.5$ and $\gamma = 1$ in Fig.6a should correspond to a linear trend in $M^2(H/M)$ coordinates in the mean-field model describing classical collinear ferromagnet. The obvious failure of the mean field model is probably due to non collinear spin structure in Ho, in contrast with simple collinear ferromagnet. Mean field theory does not describe helical or spiral spin ordering.

Convenient treatments based on 3D-Heisenberg, 3D-Ising, Tricritical models should be applied. In MnSi [28], FeGe [29], Cr1/3NbS2 [30] chiral magnets, 3D Heisenberg model implying modified β and γ values gives nice straightening of the Arrott curves. The Arrott plot is valid in the mentioned above non collinear chiral ferromagnets at the convenient parameter values, because spin Hamiltonian includes all components of exchange interaction, including asymmetric components.

The problem of Arrott plot interpretation in Ho is multiple spin transitions following one by another in temperature scale. The absence of the parallel lines in Fig.6a is also due to few transitions in studied temperature range. Change of the slope in the $M^2(H/M)$ coordinates reveals change of spin configuration.

The Arrott plot in Fig.6a overlaps at least two transitions between three spin configurations. The dashed lines in Fig.6a separate areas with different slopes. These lines are the borders separating helifan/helix and spin-slip/helix transitions. For that reason, one should analyze upper and bottom parts of the Arrott plot separately. We selected the narrow 70 - 120 K range and the 3D-Heisenberg parameters $\beta = 0.365$ and $\gamma = 1.336$ [13] providing good straightening of the curves in Arrott plot (Fig. 6b). The Arrott plot in other coordinates corresponding to 3D-Ising and Tricritical models are shown in Fig. S8 in the Supplementary material, as well as comparison with mean field model (Fig. S8 a), inconvenient for our system. All three models considering x, y, z spin projections (Fig. S8 b, c, d) give straightening at the expected β and γ values, in contrast with the mean field model (Fig. S8 a). In this part of Arrott plot, all curves can be presented as straight parallel lines indicating a second order spin transition between 70 -120 K. This temperature range corresponds probably to helifan/helix spin transition. Thus, fragmentary analysis of the Arrott plot allowed us to distinguish spin transition resolved in $1/\chi$ plot and determine the type of the transition.

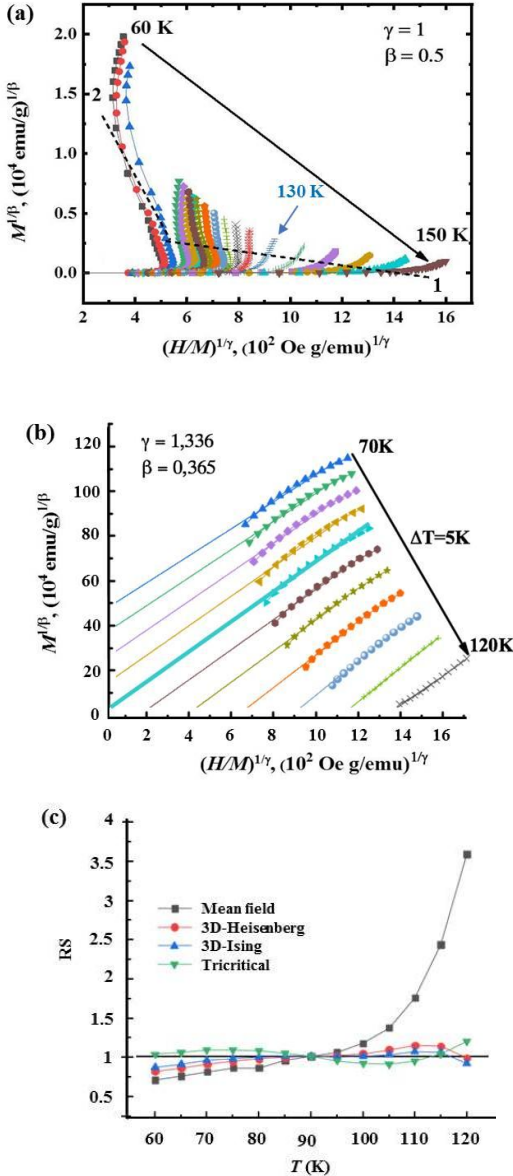


FIG.6. (a) Arrott plots $M^2(H/M)$ for the mean field $\beta = 0.5$ and $\gamma = 1$ parameters. The lines 1 and 2 are borders of the helifan-helix and spin-slip - helix transitions. Direction of the temperature change is shown by the black arrow. (b) The Arrott plot corresponding to Heisenberg model in selected temperature range possessing single phase transition at 50 K. (c) Temperature dependences of the normalized relative slopes $RS = S(T)/S(T_C)$ for Mean field, 3D-Heisenberg, 3D-Ising and Tricritical models.

The normalized relative slope $RS = S(T)/S(T_C)$ identifies the most suitable model by comparing experimental RS value with the idealized value “1”, as it was determined for the chiral FeGe alloy [29]. Plots of RS vs T for the four different models are shown in Fig. 6c. One can see that the RS of 3D-Heisenberg, 3D-Ising and Tricritical models are close to ‘1’, while that of the Mean field model is far from ‘1’ above 90 K. This result indicates that the critical behavior of Ho may not belong to a single universality class. Although, mean field coordinates do not result in correct Arrott plot, they give correct value of the early known paramagnet-helix spin transition at 132 K (shown by arrow), where the negative slope changes to positive slope (Fig. 6 a).

D. Change of magnetic part of entropy accompanying spin transitions

The basic principal determining entropy calculation is Maxwell’s equation connecting changes of entropy and magnetic moment [31]:

$$\left(\frac{\partial S}{\partial H}\right)_T = \left(\frac{\partial M}{\partial T}\right)_H \quad (4)$$

The Maxwell’s equation (4) refers to the total entropy S including phonon, electronic and magnetic parts. In a first order transition S, V and M are discontinuous and the Maxwell equation collapses into Clausius-Clapeyron equation:

$$\Delta S/\Delta M = -dH/dT \quad (5)$$

which is rigorously valid to calculate change of magnetic part of the entropy ΔS_M , if temperature hysteresis is absent [31]. In Ho crystal no structural transitions were observed in 2-300 K range. In contrast with the shape memory Heusler alloys, described in [31], Ho crystal does not manifest strong contribution of magneto-elastic energy. First order transitions can be observed at low temperatures ~ 2 K [32]. Temperature range analyzing in our experiments is free of first order transitions [32]. Thus, one can conclude validity of the Eqn. (5) to determine magnetic part of the entropy. Series of the isothermal magnetization curves corrected by the determined demagnetizing factor (Fig. S5) were used to calculate magnetic part of entropy S_M and its variation $\Delta S_M(H, T)$, caused by spin-reorientation transitions (Fig. 7).

The expression for calculation of magnetic part of the entropy can be obtained from (5):

$$\Delta S_M(T, H) = \int_0^H \left(\frac{\partial M(T, H)}{\partial T} \right)_H dH \quad (6)$$

Since temperature and magnetic field were discretely changed in our experiments, Eqn.(6) can be rewritten, as given below, as a sum of several discrete contributions:

$$\Delta S_M(T, H_0) = \sum_i \frac{M_{i+1}(T_{i+1}, H) - M_i(T_i, H)}{T_{i+1} - T_i} \quad (7)$$

$M_i(T_i, H)$ is the magnetic moment at temperature T_i , corresponding to i -th field dependence, $M_{i+1}(T_{i+1}, H)$ is the magnetic moment at temperature T_{i+1} corresponding to neighboring $i+1$ -th field dependence (Fig. 5). Plots of $\Delta S_M(H, T)$ dependences calculated for the in-plane and out-of-plane field orientations are shown in Fig. 7(a) and Fig. 7(b), respectively.

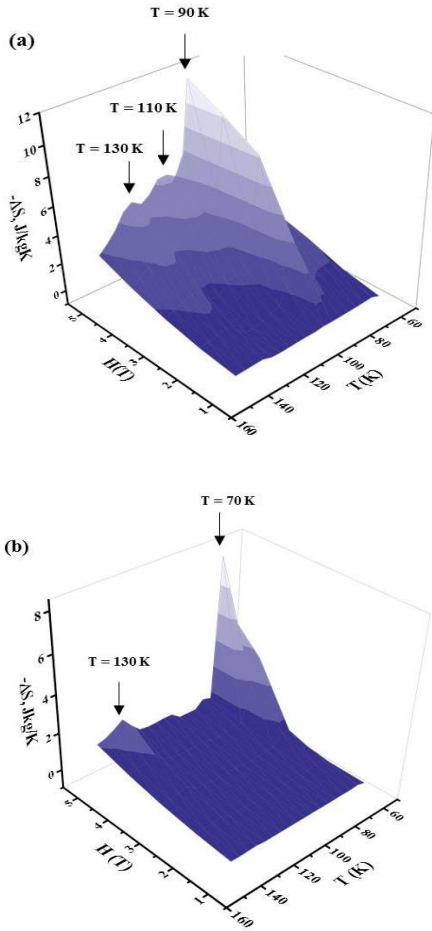


FIG.7. Change of magnetic entropy ΔS_M in the in- plane (a) and out-of-plane (b) orientations.

Figure 7 shows the magnetic entropy change obtained from isothermal field dependencies of the magnetization $M(H)$ by applying Eqn.(7). Maximal entropy change $-\Delta S_M = 11.8$ J/kgK was observed at 90 K for in-plane applied field orientation (Fig. 7(a)) and $-\Delta S_M = 8.2$ J/kgK at 70 K for out-of-plane applied field orientation (Fig. 7(b)) under 5 T magnetic field. Expected maximum of the $\Delta S_M(T)$ dependence at $T_N = 130$ K corresponding to helix-paramagnet transition has a same position for both the perpendicular and the parallel field orientations. Maximal change of the entropy $-\Delta S_M$ does not exceed 5 J/kgK for in-plane

orientation and 2 J/kgK for perpendicular orientation at $T_N = 130$ K.

Thus, spin-reorientation transitions at 90 K at 5 T and transition at 70 K demonstrate that the observed MCE is quite significant even when compared to the one measured for paramagnet-helix spin transition. This fact attracts interest to Ho film in intermediate temperature region 70 - 110 K.

E. Anisotropy of the H - T phase diagram

Spin-reorientation transitions in Ho are mainly driven by magneto-crystalline anisotropy caused by mixing of electron levels of Ho^{3+} ions depending on crystallography orientation [33]. The magneto-crystalline single axis anisotropy of Ho is very high ($K_I = -1.45 \times 10^8$ erg/cm³) due to the orbital wave function of Ho, with high $L = 6$ orbital moment sensitive to the crystal field of other atoms. Anisotropy in the phase diagram results of the large magneto-crystalline anisotropy energy which is comparable with the exchange energy [34]. Holmium exhibits very high ellipsoidal magnetostriction with maximal value of 2500 ppm along c axis at 4 K [34]. In our work, we observe strong difference in MCE and other magnetic properties between magnetic fields applied parallel and perpendicular to the c -axis. The summarized magnetic phase diagrams of our sample for those two orientations are shown in Fig. 8.

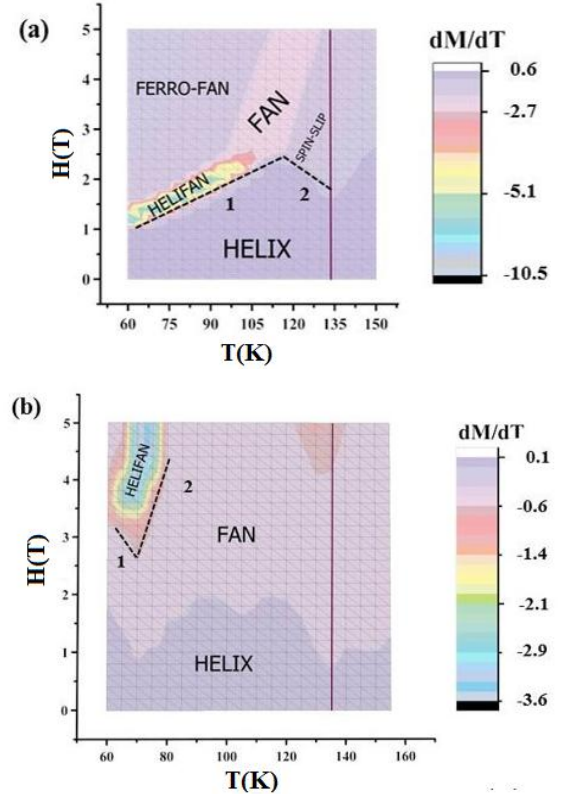


FIG.8. Magnetic phase diagram of W/Ho/W/MgO sample for in-plane (a), out-of-plane (b) field orientations. The lines 1 and 2 correspond to helifan-helix and spin-slip-helix transitions.

According to [8] helical phase transforms to fan at $T = 70$ K with out-of-plane magnetic field, while helicoidal structure transforms to helifan state at $T = 90$ K under the influence of magnetic field applied in the plane of the sample. Since the $H(M, T)$ diagram was corrected from the demagnetizing field, the

difference between the two orientations cannot be explained by shape anisotropy and is related to the magneto-crystalline anisotropy of Ho in the stress extended film.

Anisotropy of the MCE was early observed in many alloys [35-40]. It has been reported [35], that $-\Delta S_M$ changes under rotating the sample in the applied magnetic field. It has been shown in Ref. [36] that the entropy change is two times larger for $H//[110]$, than for $H//[100]$ field direction.

An increase of $-\Delta S_M$ with a change in the direction magnetic field orientation was found in $\text{Fe}_{3-x}\text{GeTe}_2$ [37]. The periodicity of angular dependence of the MCE was found in [38, 39]. Giant anisotropy of magnetocaloric effect in TbMnO_3 single crystals between different axes was found [40]. These findings relate to the first order transitions near the Curie point. However, the results presented in this paper for the case of Ho film demonstrate similar anisotropic MCE due to second order spin-reorientation transitions.

For practical applications of the MCE require materials with higher value for relative cooling power (RCP) as well as for entropy (see Fig. S9 in the Supplementary material [13]). In order to verify this, we have calculated the RCP values that depend on ΔS_M as well as on shape of the $\Delta S_M(T)$ curve.

The calculations are done by the formula $RCP = -\Delta S_M \delta T_{FWHM}$, where δT_{FWHM} is Full Width at Half Maxima of the $-\Delta S_M(T)$ curve [41]. The RCP value for in-plane field orientation are two times higher than for out-of-plane orientation (see Fig. S9 in Supplementary material [13]). Relative RCP cooling power in MgO/W/Ho (400 nm)/W films at 5 T reaches 120 TJ/kgK for in-plane and 60 TJ/kgK for perpendicular orientation of the applied magnetic field.

IV. CONCLUSIONS

The magnetocaloric effect in the multilayer MgO/W/Ho (400nm)/W structure of (0002) Ho orientation has been investigated near the spin reorientation temperatures. Under in plane applied magnetic field the magnetocaloric effect, observed at 130 K is 2.5 times greater than that observed for the case when field was applied out-of-plane. With the sample magnetization oriented parallel to the external magnetic field, the transition between metastable magnetic structures from helix to helifan at $T = 90$ K results in entropy change $\Delta S_M = -11.8$ J/kgK in a field of 4 T. In a perpendicular magnetic field orientation, the maximum ΔS_M shifts to low temperature region. At $T = 70$ K, the maximum change in entropy is $\Delta S_M = -8.2$ J/kgK, which can be explained by the transition of the helix structure to fan one. Remarkable change of the helifan and fan areas in H - T diagram due to orientation allows one to choose in-plane orientation of field to reach the highest change of dM/dT value at easy accessible field ~ 1 T and temperature ~ 100 K. We also verified borders separating helifan/helix and spin-slip/helix transitions in Arrott plot.

Furthermore, we have shown that the relative RCP cooling power in MgO/W/Ho (400 nm)/W films at 5 T reaches 120 TJ/kgK for in-plane and 60 TJ/kgK for perpendicular orientation of the applied magnetic field. The anisotropy dependent magnetocaloric effect in holmium opens up new possibilities for controlling and optimizing the magnetocaloric effect in thin magnetic films.

ACKNOWLEDGMENTS

We acknowledge funding from the Ministry of Science and Higher Education of the Russian Federation (Grant No. 13.1902.21.0006). R. M. was supported by «Project for enhancing of competitiveness of leading Russian universities among leading research and educational centres (5–100)».

REFERENCES

1. T. Chatterji *Neutron scattering from magnetic materials, Chapter 2: Magnetic Structures* (Elsevier, 2006). <https://doi.org/10.1016/B978-044451050-1/50003-3>
2. W.C. Koehler, J. W. Cable, H. R. Child, M. K. Wilkinson, and E. O. Wollan, *Phys. Rev.* **158**, 450 (1967). <https://doi.org/10.1103/PhysRev.158.450>
3. N. Ali, F. Willis, M. O. Steinitz, M. Kahrizi, and D. A. Tindall, *Phys. Rev. B* **40**, 11414 (1989). <https://doi.org/10.1103/PhysRevB.40.11414>
4. D.A. Tindall, M. O. Steinitz, and M. L. Plumer, *Phys. F: Metal. Phys.* **7**, L263 (1977). <https://doi.org/10.1088/0305-4608/7/9/005>
5. J. Bohr, D. Gibbs, D. E. Moncton, and K. L. D'Amico, *Phys. A* **140**, 349 (1986). [https://doi.org/10.1016/0378-4371\(86\)90241-4](https://doi.org/10.1016/0378-4371(86)90241-4)
6. L. J. Rodrigues, V. D. Mello, D. H. A. L. Anselmo, and M. S. Vasconcelos, *J. Magn. Magn. Mat.* **377**, 24 (2015). <https://doi.org/10.1016/j.jmmm.2014.10.027>
7. R. A. Cowley, P. M. Gehring, D. Gibbs, J. P. Goff, B. Lake, C. F. Majkrzak, A. Vigliante, R. C. C. Ward, and M. R. Wells, *J. Phys.: Cond. Mat.* **10**, 6803 (1998). <https://doi.org/10.1088/0953-8984/10/30/018>
8. V. I. Zverev, A. M. Tishin, Z. Min, Y. Mudryk, K. A. Gschneidner Jr, and V. K. Pecharsky, *J. Phys.: Condens.Mat.* **27**, 146002 (2015). <https://doi.org/10.1088/0953-8984/27/14/146002>
9. H. N. Bez, A. K. Pathak, A. Biswas, N. Zarkevich, V. Balema, Y. Mudryk, D. D. Johnson, and V. K. Pecharsky, *Acta Mat.* **173**, 225 (2019). <https://doi.org/10.1016/j.actamat.2019.05.004>
10. J. Liu, T. Gottschall, K. P. Skokov, J. D. Moore, and O. Gutfleisch, *Nature Mat.* **11**, 620 (2012). <https://doi.org/10.1038/nmat3334>
11. I. D. Rodionov, D. E. Mettus, A. P. Kazakov, M. V. Prudnikova, V. N. Prudnikov, I. S. Dubenko, and A. B. Granovsky, *Phys. of the Sol. St.* **55**, 1861 (2013). <https://doi.org/10.1134/S1063783413090266>
12. T. D.Thanh, D. C. Linh, P. D. H. Yen, L. V. Bau, V. H. Ky, Z. Wang, H.G. Piao, N. M. An, and S.C. Yu, *Phys. B: Condens. Matt.* **532**, 166 (2018). <https://doi.org/10.1016/j.physb.2017.03.031>
13. See Supplemental Material at <http://link.aps.org/supplemental/> for MS Word file containing sketches of the sample structure and Ho magnetic structures, XPS spectra and sketch of determined X-ray penetration depths, EDX spectrum, fragments of Arrott plots within field ranges corresponding to the single magnetic phase, magnetic hysteresis, FC-ZFC curves and reciprocal susceptibility temperature plot for two

- orientations, demonstration of demagnetizing field effect, field dependence of RCP factor and correspondent captions for all mentioned figures.
14. D. L. Strandburg, S. Legvold, and F. H. Spedding, *Phys. Rev.* **127**, 2046 (1962). <https://doi.org/10.1103/PhysRev.127.2046>
 15. J. Bohr, D. Gibbs, D.E.Moncton, and K.L.D'Amico, *Phys. A*, **140** 349 (1986). [https://doi.org/10.1016/0378-4371\(86\)90241-4](https://doi.org/10.1016/0378-4371(86)90241-4)
 16. C.Schüßler-Langeheine, E.Weschke, A.Yu.Grigoriev, H.Ott, R.Meier, D.V.Vyalikh, C. Mazumdar, C.Sutter, D.Abernathy, G.Grübel, and G.Kaindl, *J. Electron Spectroscopy and Related Phen.* **114–116**, 953 (2001). [https://doi.org/10.1016/S0368-2048\(00\)00318-2](https://doi.org/10.1016/S0368-2048(00)00318-2)
 17. E. E. Fullerton, C. H. Sowers, J. P. Pearson, X. Z. Wu, D. Lederman, S. D. Bader, *Structure and magnetism of epitaxial rare-earth-transition-metal films* in *Magnetic Hysteresis in Novel Magnetic Materials*, Ed.: G.C. Hadjipanayis, (Kluwer Academic Press, Netherlands, 1997), pp. 467-478. <https://www.osti.gov/servlets/purl/390625>
 18. V. Leiner, D. Laberge, R. Siebrecht, Ch. Sutter, and H. Zabel, *Phys. B* **283**, 167 (2000). [https://doi.org/10.1016/S0921-4526\(99\)01923-7](https://doi.org/10.1016/S0921-4526(99)01923-7)
 19. P.Szary, D. Kaiser, J.Bick, D. Lott, A.Heinemann, C.Dewhurst, R. Birringer and A. Michels, *J. Appl. Cryst.* **49**, 533 (2016). <http://dx.doi.org/10.1107/S1600576716001898>
 20. Crystallography Open Database <https://www.crystallography.net/cod/9008502.html>
 21. V. Tarnavich, A. Volegov, D. Lott, S. Mattauch, A. Vorobiev, A. Oleshkevych, and S. Grigoriev, *J. Surf. Invest.* **8**, 976 (2014). <https://doi.org/10.1134/S1027451014050425>
 22. K. Kanaya, S. Okayama, Penetration and energy-loss theory of electrons in solid targets, *Physics D: Applied Physics*, **5** (1972), pp. 43–58. <https://doi.org/10.1088/0022-3727/5/1/308>
 23. M. Bratko, K. Morrison, A. de Campos, S. Gama, L. F. Cohen, and K.G. Sandeman, *Appl. Phys. Lett.* **100**, 252409 (2012). <https://doi.org/10.1063/1.4729893>
 24. D. X. Chen, E. Pardo, and A. Sanchez, *IEEE Trans. Magn.* **38**, 1742 (2002). <https://doi.org/10.1109/TMAG.2002.1017766>
 25. S. Chikadzumi, Ed. C. D. Jr. Graham *Physics of ferromagnetism* (Clarendon, Oxford 1997). <https://global.oup.com/academic/product/physics-of-ferromagnetism-9780198517764?cc=ru&lang=en&#>
 26. I. Yeung, R. M. Roshko, and G. Williams, *Phys. Rev. B* **34**, 3456 (1986). <https://doi.org/10.1103/PhysRevB.34.3456>
 27. B. K. Banerjee, *Phys. Lett.* **12**, 16 (1964). [https://doi.org/10.1016/0031-9163\(64\)91158-8](https://doi.org/10.1016/0031-9163(64)91158-8)
 28. M. K. Chattopadhyay, P. Arora and S. B. Roy, *J. Phys.: Condens. Matter*, **21**, 296003 (2009). <https://doi.org/10.1088/0953-8984/21/29/296003>
 29. L. Zhang, H.Han, M. Ge, H. Du, C. Jin, W. Wei, J. Fan, C. Zhang, L. Pi & Y. Zhang, *Scientific Reports*, **6**, 22397(2016). <https://doi.org/10.1038/srep22397>
 30. E. M. Clements, R. Das, L. Li, P. J. Lampen-Kelley, M.Phan, V. Keppens, D. Mandrus & H.Srikanth, *Scientific Reports*, **7**, 6545 (2017). <https://doi.org/10.1038/s41598-017-06728-5>
 31. A. Planes, L.Manosa and M. Acet, *J. Phys.: Condens. Matter* **21**, 233201 (2009). <https://doi.org/10.1088/0953-8984/21/23/233201>
 32. M. L. Plumer, *Phys. Rev. B* **44**, 12376 (1991). <https://doi.org/10.1103/PhysRevB.44.12376>
 33. H. Ohsumi, *J. Phys. Soc. Jpn.* **71**, 1732 (2002). <https://doi.org/10.1143/JPSJ.71.1732>
 34. J. J. Rhyne, S. Foner, E. J. McNiff Jr., and R. Doclo, *J. Appl. Phys.* **39**, 892 (1968). <https://doi.org/10.1063/1.1656324>
 35. Yu Liu, and C. Petrovic, *Phys. Rev. B* **97**, 174418 (2018) <https://doi.org/10.1103/PhysRevB.97.174418>
 36. D.X.Li, S.Nimori, and T.Shikama, *Solid State Comm.* **150**, 1865 (2010). <https://doi.org/10.1016/j.ssc.2010.07.049>
 37. Yu Liu, J. Li, J. Tao, Y. Zhu, and C.R. Petrovic, *Sci. Rep.* **9**, 13233 (2019). <https://doi.org/10.1038/s41598-019-49654-4>
 38. V. I. Ivanovskii, and P. P. Denisov, *Sov. Phys. Journ.* **9**, 88 (1966). <https://doi.org/10.1007/BF00818749>
 39. K. P. Skokov, Y. G. Pastushenkov, S. A. Nikitin, M. Fries, and O. Gutfleisch, *IEEE Trans. Magn.* **52**, 1 (2016). <http://dx.doi.org/10.1109/TMAG.2016.2530138>
 40. J.Y. Moon, M.K. Kim, D.G. Oh, J.H., Kim H.J. Shin, Y.J. Choi, and N. Lee. *Phys. Rev. B.* **98**, 174424 (2018). <https://doi.org/10.1103/PhysRevB.98.174424>
 41. K. A. Gschneidner, V. K. Pecharsky, and A. O. Tsokol, *Rep. Prog. Phys.* **68**, 1479 (2005). <https://doi.org/10.1088/0034-4885/68/6/R04>